

# Where Galaxies Point: First Measurement of the Large-Scale Axial Intrinsic Alignment

Pedro da Silveira Ferreira,<sup>1,2,3,\*</sup> Rafael Oliveira Ramos,<sup>4</sup> Paula S. Ferreira,<sup>5,1</sup>  
Arianna Cortesi,<sup>4,3</sup> Fabricio Ferrari,<sup>6</sup> Valerio Marra,<sup>7,8,9</sup> and Clécio R. Bom<sup>2</sup>

<sup>1</sup>*Center for Cosmology and Computational Astrophysics,*

*Institute for Advanced Study in Physics, Zhejiang University, Hangzhou 310058, China.*

<sup>2</sup>*Centro Brasileiro de Pesquisas Físicas, 22290-180, Rio de Janeiro, RJ, Brazil*

<sup>3</sup>*Observatório do Valongo, Universidade Federal do Rio de Janeiro, 20080-090, Rio de Janeiro, RJ, Brazil*

<sup>4</sup>*Instituto de Física, Universidade Federal do Rio de Janeiro, 21941-972, Rio de Janeiro, RJ, Brazil*

<sup>5</sup>*Observatório Nacional, 20921-400, Rio de Janeiro, RJ, Brazil*

<sup>6</sup>*Instituto de Matemática Estatística e Física, Universidade Federal do Rio Grande, 96203-900, Rio Grande, RS, Brazil*

<sup>7</sup>*Departamento de Física, Universidade Federal do Espírito Santo, 29075-910, Vitória, ES, Brazil*

<sup>8</sup>*INAF – Osservatorio Astronomico di Trieste, via Tiepolo 11, 34131, Trieste, Italy*

<sup>9</sup>*IFPU – Institute for Fundamental Physics of the Universe, via Beirut 2, 34151, Trieste, Italy*

(Dated: November 25, 2025)

Applying a new estimator to the Dark Energy Survey (DES) Y3 weak lensing shape catalog, we map the galaxies' orientation field and report the first detection of a large-scale axial intrinsic alignment (LAIA) on dipolar angular scales. Ellipticals' semi-major axes and spirals' semi-minor axes coherently point toward a common direction,  $(\text{RA}, \text{Dec}) = (306_{-4}^{+6}, 52_{-3}^{+3})^\circ$  and  $(296_{-18}^{+10}, 50_{-2}^{+6})^\circ$ , respectively, with amplitudes in the expected tidal-torquing hierarchy. This pattern could be produced by a horizon-scale tidal field imprinted by primordial inhomogeneities during galaxy assembly and, if confirmed, would signal a statistically significant preferred direction in the Universe, thereby probing deviations from statistical isotropy. The signal persists across spatial and redshift splits and is difficult to attribute to survey systematics. LAIA offers a new sky-wide compass linking galaxy evolution and cosmology.

## I. INTRODUCTION

Galaxies exhibit correlations in their orientations and shapes within their neighborhood, known as intrinsic alignments (IA) [1, 2]. These arise from tidal interactions with the surrounding large-scale filamentary structure, influencing galaxy formation and evolution. While weak gravitational lensing seeks to measure the distortions of galaxy shapes caused by intervening mass, IA can introduce a spurious signal that mimics or obscures the true lensing-induced correlations. This contamination becomes critical in cosmic shear studies, where precise measurements of the lensing signal are used to infer cosmological parameters and the nature of dark energy. Consequently, accurate modeling and mitigation of IA are essential to control systematics in weak lensing analyses and ensure robust cosmological constraints [3–5].

Beyond its impact on cosmic shear, IA also provides a unique window into galaxy formation and the role of large-scale tidal fields in shaping galactic structures [4–13]. Observational evidence suggests that galaxy orientations can become correlated over scales up to  $\sim 100$  Mpc/ $h$  due to coherent tidal forces, leading to measurable large-scale alignment patterns. These correlations constrain models of structure formation by encoding the interplay between dark matter halos, baryonic processes, and the cosmic web [11, 14], and can probe primordial

non-Gaussianity (PNG) [15, 16]. Thus, while IA is often viewed as a contaminant in weak lensing surveys, it also constitutes a valuable probe of the underlying astrophysical processes governing galaxy evolution and the young inflating Universe.

On even larger scales, as upcoming surveys such as China Space Station Telescope (CSST) [17], Legacy Survey of Space and Time (LSST) [18] and *Euclid* [19] gather unprecedented data, the understanding and modeling of IA will become increasingly important. The combination of high-precision cosmic shear measurements, spectroscopic galaxy clustering, and other cosmological observables promises to tightly constrain cosmological models. In parallel, a more robust theoretical and simulation-based framework for IA will be critical for consistently interpreting these data and extracting maximal information from them [4, 20]. The success of forthcoming surveys, therefore, hinges on rigorous IA treatments that balance statistical precision with systematic control, enabling us to fully exploit the weak lensing signal.

From large-scale structure (LSS) data sets, the first detection of IA in galaxy surveys by Brown *et al.* [21] used the SuperCOSMOS Sky Survey and found a high correlation between the galaxies' ellipticities for small angular scales (1–100 arcmin). On larger scales, Smargon *et al.* [22] used data from the Sloan Digital Sky Survey (SDSS) to find IA between pairs of clusters, and concluded that there was indeed IA over 1–100 Mpc/ $h$  scales, but weaker than theory predicts. Recently, a new approach using the Dark Energy Spectroscopic Instrument (DESI) data employs galaxy multiplets to measure IA with respect to

\* [dasferreira.pedro@gmail.com](mailto:dasferreira.pedro@gmail.com)

a tracer sample over 1–100Mpc/ $h$  scales [23]. They report agreement with mocks and, for  $\gtrsim 20$  Mpc/ $h$ , with nonlinear theory, providing evidence for large-scale IA.

We can go one step further and ask whether IA persists on even larger scales, up to the Universe as a whole. If the matter in the Universe is distributed in such a way that a particular direction is favored, that is, if there is an excess of matter along one orientation, a large-scale dipolar gravitational field may arise. This dipole could generate an enhanced alignment in galaxy orientations, indicating a preferred direction. This scenario is inconsistent with the cosmological principle, which states that the Universe is statistically homogeneous and isotropic on scales larger than about 100–200 Mpc/ $h$  [24, 25]. Searching for such a dipole therefore directly tests this assumption. See also forecasts for a primordial dipolar power modulation jointly probed with clustering and IA [26].

Since aberration from our motion leaves galaxy shapes unchanged [27], and full-sky weak-lensing shear cannot produce a genuine dipole in orientations because it stretches images in alternating patterns that cancel when averaged over hemispheres, any apparent dipole in galaxy orientations must arise from survey geometry and mode mixing rather than shear itself. By contrast, lensing magnification changes sizes and number counts and can vary across the sky in a way that appears dipolar, but it does not rotate position angles [28]. Consequently, dipolar-scale intrinsic alignments are independent of peculiar motion and are likely only weakly affected by lensing. While tidal-alignment models successfully describe large-scale IA, there is still no consolidated theoretical prediction for the amplitude of a genuinely dipolar IA [10, 29, 30]. We therefore test the null hypothesis by comparing the observed distribution of galaxy position angles with random realizations under the survey mask.

The most conservative explanation for a dipole-scale IA is the linear, or tidal-alignment, response of galaxy shapes to a long-wavelength gravitational potential. In this picture, first formulated by Catelan *et al.* [31], the local halo shape (or angular-momentum tensor) is “frozen in” by the ambient tidal field at galaxy formation. A robust measurement of a large-scale IA would therefore provide direct evidence of the tidal tensor, independent of weak-lensing shear. That is, it could detect imprints of primordial anisotropy and tidal fields during the reionization era. More speculatively, a dipolar IA signature could carry the imprint of primordial physics that breaks statistical isotropy. Some inflationary scenarios generate anisotropic PNG, inducing a scale-dependent “tidal” bias in galaxy shapes and orientations [15].

Detecting a large-scale axial IA (LAIA), i.e. an alignment toward a direction on the sky, therefore offers a novel test of primordial physics, complementary to CMB anomalies and large-scale galaxy number counts, and can help discriminate between isotropic slow-roll inflation and models with direction-dependent initial conditions. In this work, we propose a methodology to estimate the LAIA and obtain its first measurement.

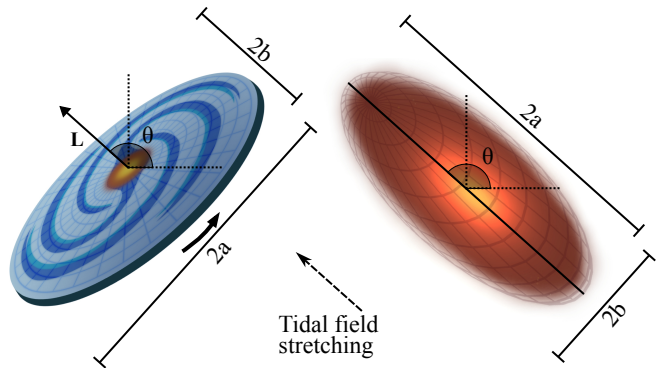


Figure 1. **Left)** Spiral galaxies tend to align their angular-momentum vector  $\mathbf{L}$  with the tidal field. The projection of  $\mathbf{L}$  onto the image plane corresponds to the observed minor axis (b) direction. **Right)** By contrast, elliptical galaxies typically align their major axes (a). Thus, under the same tidal field, spirals and ellipticals become orthogonal on average.

## II. LARGE-SCALE AXIAL INTRINSIC ALIGNMENT (LAIA)

IA refers to correlations in galaxy orientations that arise from structure formation rather than gravitational lensing. Conceptually, the same large-scale tidal fields that shape the cosmic web can imprint preferred orientations on galaxies, producing coherent patterns across tens of megaparsecs. Commonly, early-type (elliptical) galaxies respond primarily to a linear coupling between their pressure-supported stellar distributions and the ambient tidal field, while late-type (spiral) galaxies respond mainly to tidal torquing, in which a proto-galactic inertia tensor couples quadratically to the tides to generate correlated spins [1, 2]. Contemporary formalisms such as the nonlinear alignment (NLA) [3, 34], and the tidal-alignment and tidal-torquing (TATT) models [35] provide a unified language for these phenomena and for their scale and redshift dependence, while observational analyses routinely separate lensing from IA via two-point statistics of shapes and their cross-correlations with density. In this picture, IA is not a single effect but a family of mechanisms whose relative importance depends on morphology, color, mass, and environment [1–5, 14, 30, 31, 36, 37].

The elliptical versus spiral distinction matters both physically and observationally. For ellipticals, the linear response tends to align galaxy major axes with the local tidal eigenframe, yielding long-range coherence in projected shapes that is strongest for red, luminous, and high-mass galaxies [4, 5, 38, 39]. For spirals, the primary correlation is between spin and the surrounding filaments and walls: tidal torques align the angular momentum vector of the galaxy with features of the cosmic web. Fig. 1 summarizes the effects: spiral galaxies tend to align their angular-momentum vector  $\mathbf{L}$  with the tidal field, while elliptical galaxies typically align their major axis. See Chisari [1] for an overview of IA theory. Moreover, be-

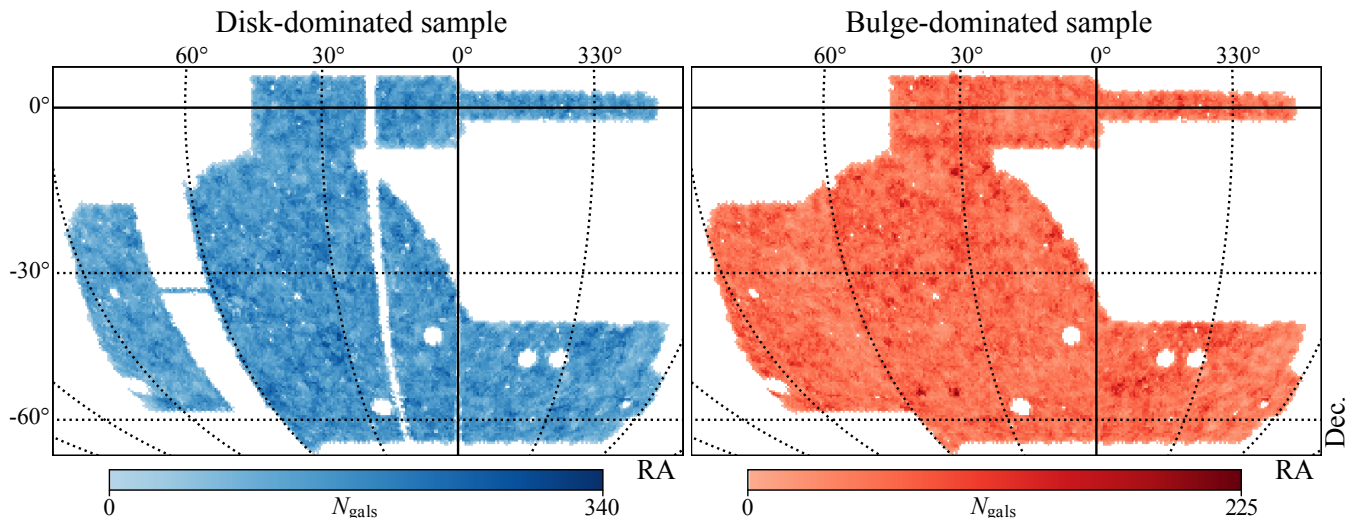


Figure 2. **Left)** Mollweide projection map in equatorial coordinates of the disk-dominated sample (DD), i.e. late-type (spiral), density and footprint considering HEALPix NSIDE=128 resolution. **Right)** The same for the bulge-dominated sample (BD), i.e. early-type (elliptical). Footprint differences reflect the different sky coverage of the classification catalogs [32, 33].

cause spin alignments arise from quadratic couplings to the tidal field, the expected signal from spirals is suppressed relative to the linear response of ellipticals, explaining why spiral IA in standard shape–density statistics is typically weaker [4, 31, 35], though spin–filament alignments are evident in simulations and environmental measurements [38, 40–42].

In practice, here we divide galaxies into bulge-dominated and disk-dominated systems, since pressure support versus rotational support sets the operative mechanism (linear response versus torquing). For disk-dominated systems we also adopt the thin-disk approximation: late-type galaxies have small intrinsic thickness, so position angle and apparent axis ratio mainly trace viewing angle and spin direction [43]. To obtain classified samples with precise position angles (PAs), we use the Dark Energy Survey (DES) Y3 shape catalog [44], whose provided ellipticity components have the PSF anisotropy deconvolved with high precision by the `metacalibration` (MC) algorithm [44]. This catalog is crossed with the robust morphological classifications made by Vega-Ferrero *et al.* [32] and Cheng *et al.* [33], and bulge-to-total fraction (BDF) constraints [45]. In addition, we impose a threshold on the PA uncertainty,  $\sigma_\theta < 5^\circ$ , to avoid possible residual PSF bias in galaxies with ellipticity  $\sim 1$  and artifacts that render the PA fit unstable. Furthermore, a low-depth decision tree, based on visual inspection of 10 000 objects images, was used to derive simple piecewise thresholds to separate residual artifacts/blends from galaxies. Moreover, the visual inspection sample was used to ensure that we used the correct reference frame (World Coordinate System) and check PA consistency (see Fig. 5), by comparison between the ones measured visually, using the MORFOMETRYKA software [46] and by MC. The complete sample selection is described in details in App. A. See Fig. 2 for the density HEALPix [47] map

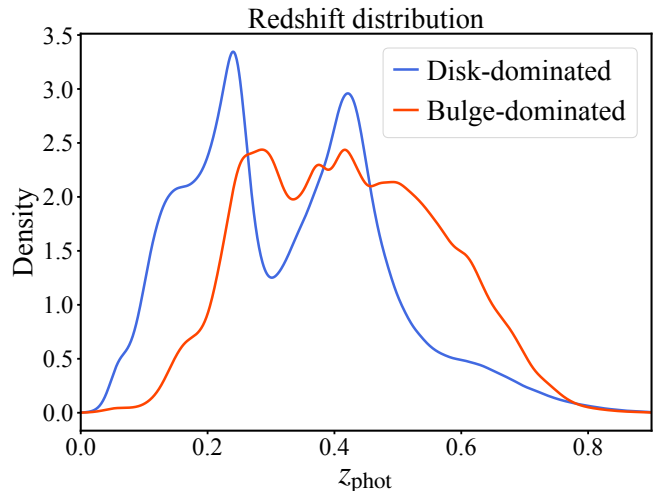


Figure 3. Photometric redshift distribution of each sample.

distribution of the disk-dominated sample (DD) and the bulge-dominated sample (BD), and Fig. 3 for the redshift distribution.

Most IA measurements target two-point functions that probe correlation as a function of separation. Here we seek a different observable: the LAIA, a large-scale axial signal, namely a single sky direction  $\hat{\mathbf{d}}$  that maximizes the net alignment of galaxy position angles. Considering the major-axis directions  $\hat{\mathbf{a}}_i$  and the minor axis directions  $\hat{\mathbf{b}}_i$ , with  $i$  indexing galaxies, this means we are interested in the mean squared projections  $\langle (\hat{\mathbf{d}} \cdot \hat{\mathbf{a}}_i)^2 \rangle$  and  $\langle (\hat{\mathbf{d}} \cdot \hat{\mathbf{b}}_i)^2 \rangle$ . The square is required because the semi-axis directions are headless (axial): there is no intrinsic arrow (sense is undefined), so  $\hat{\mathbf{a}}_i \equiv -\hat{\mathbf{a}}_i$  and  $\hat{\mathbf{b}}_i \equiv -\hat{\mathbf{b}}_i$ . Thus, the LAIA of a galaxy sample can be measured with an estimator

$\hat{E}(\hat{\mathbf{d}})$  that is a weighted average of the projections w.r.t.  $\hat{\mathbf{d}}$ :

$$\hat{E}^{\text{a}}(\hat{\mathbf{d}}) = \sum_{i=1}^{N_{\text{gal}}} \frac{w_i (\hat{\mathbf{d}} \cdot \hat{\mathbf{a}}_i)^2}{1 - (\hat{\mathbf{d}} \cdot \hat{\mathbf{n}}_i)^2} \quad \text{and} \quad \hat{E}^{\text{b}}(\hat{\mathbf{d}}) = \sum_{i=1}^{N_{\text{gal}}} \frac{w_i (\hat{\mathbf{d}} \cdot \hat{\mathbf{b}}_i)^2}{1 - (\hat{\mathbf{d}} \cdot \hat{\mathbf{n}}_i)^2}, \quad (1)$$

where ‘‘a’’ is the upper-index for the semi-major vector  $\hat{\mathbf{a}}$  projection, used to estimate the LAIA for bulge-dominated samples, and ‘‘b’’ for the semi-minor vector  $\hat{\mathbf{b}}$  projection, used to estimate the alignment in disk-dominated samples, see App. B for more details. The weights  $w_i$  are written as:

$$w_i = \frac{\sigma_{\theta,i}^{-2}}{\sum_{j=1}^{N_{\text{gal}}} \sigma_{\theta,j}^{-2}}. \quad (2)$$

The  $\sigma_{\theta,i}$  is the error in the PA (Appx. C). We measure  $\hat{E}^{\text{X}}(\hat{\mathbf{d}})$ ,  $\text{X} = \{\text{a}, \text{b}\}$ , for different  $\hat{\mathbf{d}}$  following a gradient ascent optimization algorithm. The direction in which  $\hat{E}^{\text{X}}(\hat{\mathbf{d}})$  is maximum is called the LAIA direction,  $\hat{\mathbf{d}}_{\text{IA}}$ . In a statistically isotropic Universe, this should be compatible with a random PA distribution. A nonzero result therefore requires some combination of tidal gradients across the footprint, anisotropic structures, and departures from isotropy during galaxy formation.

Consider a simple model in which the large-scale tidal field present during galaxy formation induces a nearly uniform departure from random PAs across the observable Universe. Assuming that galaxies coherently rotate their semi-axis toward a common alignment direction,  $\hat{a}$  for bulge-dominated systems and  $\hat{b}$  for disk-dominated systems, we can derive, as shown in App. D, the average rotation angle  $\theta_{\text{IA}}$  with respect to  $\hat{\mathbf{d}}_{\text{IA}}$ , i.e. the LAIA amplitude, as

$$2\theta_{\text{IA}} + 2\sin(2\theta_{\text{IA}}) = \frac{2\pi}{\bar{C}} \left( \hat{E}^{\text{X}}(\hat{\mathbf{d}}_{\text{IA}}) - \frac{1}{2} \right), \quad (3)$$

where  $\bar{C} = \sum_{i=1}^{N_{\text{gal}}} w_i e^{-2\sigma_{\theta,i}^2}$ .

Our objective is not a detailed physical model but a phenomenological test: any robust deviation from the null hypothesis would be meaningful, and our estimators are constructed to detect such a dipolar trend. Finally, as we assume that intrinsic alignments are consistent with tidal-alignment/torque expectations, agreement between the  $\hat{\mathbf{d}}_{\text{IA}}$  measured using  $\hat{b}$  axis of disk-dominated galaxies and the  $\hat{\mathbf{d}}_{\text{IA}}$  measured using  $\hat{a}$  of bulge-dominated galaxies would also provide evidence for a common large-scale tidal field in the early Universe. Although this picture is well supported on scales of hundreds of Mpc, we examine whether a dipolar signal persists when extrapolated to horizon-scale modes.

Certainly, several systematics can affect our measurement. To estimate  $\hat{\mathbf{d}}_{\text{IA}}$  and  $\theta_{\text{IA}}$  we control for and propagate the following systematics: (i) lensing leakage, calibrated with the BUZZARD  $N$ -body lightcone with ray tracing [48], and modeled as a stochastic  $1'$  perturbation to

Sample	Disk-dominated			Bulge-dominated		
	$\theta_{\text{IA}}$ (')	$\alpha$ (°)	$\delta$ (°)	$\theta_{\text{IA}}$ (')	$\alpha$ (°)	$\delta$ (°)
Full	$8_{-2}^{+1}$	$296_{-18}^{+10}$	$50_{-2}^{+6}$	$42_{-3}^{+3}$	$306_{-4}^{+6}$	$52_{-3}^{+3}$
$z \leq 0.4$	$6_{-1}^{+1}$	$349_{-168}^{+21}$	$43_{-15}^{+16}$	$40_{-3}^{+5}$	$329_{-9}^{+10}$	$41_{-6}^{+4}$
$z > 0.4$	$18_{-2}^{+3}$	$285_{-9}^{+1}$	$57_{-3}^{+2}$	$48_{-5}^{+4}$	$285_{-5}^{+7}$	$60_{-1}^{+2}$
$\alpha \leq 30^\circ$	$10_{-1}^{+2}$	$221_{-9}^{+7}$	$42_{-5}^{+3}$	$37_{-4}^{+6}$	$229_{-4}^{+9}$	$39_{-3}^{+2}$
$\alpha > 30^\circ$	$8_{-2}^{+2}$	$292_{-81}^{+19}$	$49_{-21}^{+5}$	$53_{-4}^{+4}$	$355_{-9}^{+13}$	$34_{-14}^{+6}$
$\delta \leq -35^\circ$	$4_{-1}^{+2}$	$231_{-16}^{+70}$	$45_{-2}^{+17}$	$33_{-3}^{+6}$	$301_{-6}^{+6}$	$48_{-2}^{+3}$
$\delta > -35^\circ$	$10_{-2}^{+2}$	$282_{-9}^{+21}$	$68_{-3}^{+3}$	$33_{-4}^{+4}$	$292_{-9}^{+14}$	$57_{-52}^{+1}$

Table I. Results for disk- and bulge-dominated samples. Columns list the probability Highest Density Interval (68.27%) of  $\theta_{\text{IA}}$  and the preferred direction  $\hat{\mathbf{d}}_{\text{IA}}$  in equatorial coordinates ( $\alpha$  for right ascension and  $\delta$  for declination) for the full case and sub-samples (redshift, right ascension and declination cuts). Bulge- and disk-dominated galaxies have their respective semi-major and minor axis aligned on average, as predicted by a horizon-scale tidal field, and with an almost order of magnitude smaller amplitude for disk-dominated sample, expected by torquing second-order nature.

the LAIA (App. E); (ii) Possible large-scale PSF residuals, mitigated by subtracting from the  $\hat{E}(\hat{\mathbf{d}})$  map (from galaxy PAs) the component proportional to the template map built from the PSF PAs evaluated at the galaxy positions (App. F); and (iii) bias from early/late-type misclassification, treated using the mean classification probabilities (App. G). We validate the estimator with mocks that include (i) and (iii) (App. H, see Fig. 6), complemented by a spatial block bootstrap that absorbs potential position-dependent systematics as (ii) (App. I). Lastly, it is important to note that LAIA is insensitive to redshift space distortions (App. J).

### III. RESULTS AND DISCUSSION

The results for the full disk and bulge-dominated samples and their subsamples are reported in Table I, with directional contours for the full samples in the first equatorial quadrant ( $0^\circ < \alpha < 90^\circ$ ,  $0^\circ < \delta < 90^\circ$ ) shown in Fig. 4. To diagnose spatially modulated systematics, we perform ‘‘left–right’’ and ‘‘top–bottom’’ splits: right-ascension subsamples ( $\alpha \leq 30^\circ$  vs.  $\alpha > 30^\circ$ ) and declination subsamples ( $\delta \leq -35^\circ$  vs.  $\delta > -35^\circ$ ), each containing nearly half of the objects in the corresponding full sample. To assess redshift dependence, we split by redshift ( $z \leq 0.4$  vs.  $z > 0.4$ ). In all cases, uncertainties are estimated via a spatial block bootstrap (App. I), so that the error bars remain sensitive to position-dependent systematics within each split without relying on modeling. Angles are reported in arcminutes (') for  $\theta_{\text{IA}}$  and degrees (°) for  $(\alpha, \delta)$ . For consistency and ease of presentation, we report the (headless) direction of  $\hat{\mathbf{d}}_{\text{IA}}$  in the Northern celestial hemisphere. The equivalent antipodal direction

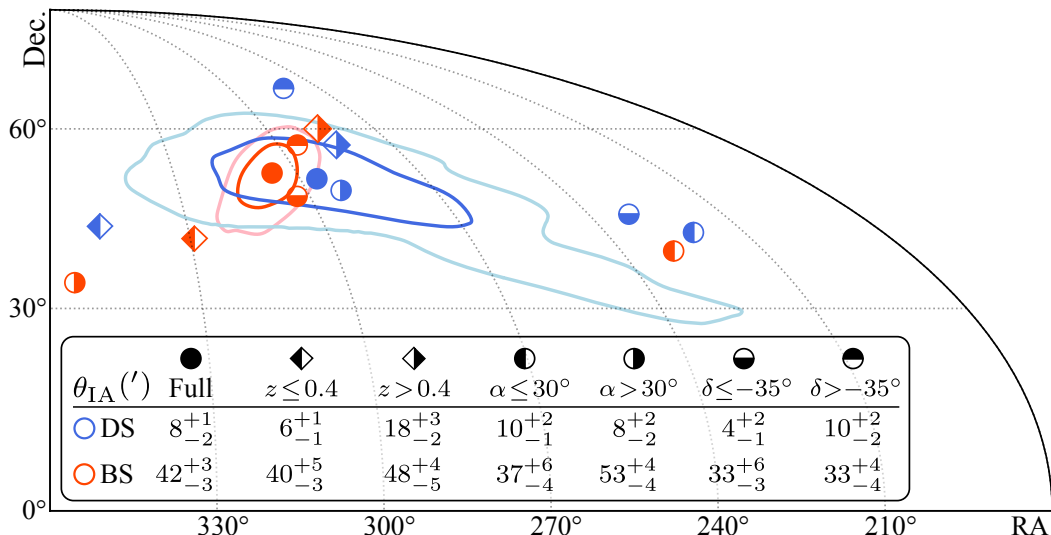


Figure 4. **Final results.** Highest-density interval (HDI) contours (68.27% and 95.45%) for the LAIA direction  $\hat{\mathbf{d}}_{\text{IA}}$  in equatorial coordinates  $(\alpha, \delta)$  for the full bulge-dominated (BD; red) and disk-dominated (DD; blue) samples. Markers show the HDI peaks for splits by redshift  $z$ , right ascension  $\alpha$ , and declination  $\delta$ . The legend lists the measured  $\theta_{\text{IA}}$  (arcminutes,  $'$ ) for the full samples and each split. Both morphologies indicate a common preferred direction, bulge major axes and disk minor axes, consistent with a large-scale tidal field, with the disk signal smaller than the bulge signal as expected from tidal torquing. The panel is restricted to the quadrant where the contours concentrate to improve readability. The antipodal direction  $(\alpha + 180^\circ, -\delta)$  is physically equivalent for this axial estimator.

in the Southern hemisphere is  $(\alpha + 180^\circ, -\delta)$ . This ambiguity is inherent to axial quantities.

Our main results are those of the full disk-dominated (DD) sample (Table I, blue), and of the full bulge-dominated (BD) sample (Table I, red). These differ from a null model including lensing leakage at  $3.2\sigma$  and  $7.9\sigma$ , respectively. We robustly detect a large-scale axial intrinsic alignment (LAIA) across the DES footprint of  $\sim 5,000 \text{ deg}^2$  ( $\simeq 12.5\%$  of the sky) over  $0 < z < 0.9$ , establishing IA on dipolar angular scales (i.e., cosmological). The contours in Fig. 4 show that, on average, bulge-dominated galaxies' semi-major axes are aligned with the disk-dominated galaxies' semi-minor axes, as expected for a horizon-scale tidal field. The DD LAIA amplitude is nearly an order of magnitude smaller than for BD, consistent with the second-order nature of tidal torquing [1–3, 5]. This morphology-dependent, orthogonal pattern over similar sky footprints is not plausibly produced by survey artifacts; reproducing it would require a highly contrived, fine-tuned systematic that aligns BD major axes and DD minor axes simultaneously. Nonetheless, the measurements are robust: they pass PSF de-leakage and lensing-leakage calibrations and early/late-type misclassification–bias removal tests, and together they constitute the first detection of LAIA. Moreover, our HDI contours do not coincide with the CMB dipole [49], large-scale anomaly axes [50], or prominent voids/attractors [51].

Across the fourteen subsamples in Table I and Fig. 4, the inferred amplitudes  $\theta_{\text{IA}}$  and preferred directions  $(\alpha, \delta)$  are largely consistent within the quoted uncertainties, with a few noteworthy deviations. In amplitude,

the DD  $z > 0.4$  split is significantly higher than both the full DD sample and the  $z \leq 0.4$  subsample. In direction, the largest shifts occur in the right-ascension splits: for BS, the two halves peak near  $\alpha \simeq 229^\circ$  and  $\alpha \simeq 355^\circ$  (cf.  $\alpha \simeq 306^\circ$  for the full BD), and for DD the  $\alpha \leq 30^\circ$  subsample shifts toward  $\alpha \simeq 221^\circ$ ; these changes are not accompanied by comparable variations in  $\delta$ , for the DD  $\delta > -35^\circ$  slice the tension is due to a higher  $\delta$  ( $68_{-3}^{+3}$ ). Crucially, the qualitative picture is unchanged across all splits: the BD major axes and the DD minor axes are mutually aligned on average, and the DD amplitude remains smaller by nearly an order of magnitude. Because the BD catalog has a  $\sim 100\times$  higher misclassification rate than DD (26.55% vs. 0.27%, App. G), BD is intrinsically more susceptible to residual systematics, which can explain the right-ascension-only shifts observed in a subset of the spatial cuts. Even allowing for a putative right-ascension systematic of  $30\text{--}60^\circ$  affecting three of the fourteen splits, the global trend and the stability of  $\theta_{\text{IA}}$  and  $\delta$  across cuts persist, and our main conclusion, the robust detection of LAIA from the full BD and DD samples, remains unaffected.

To report a physically interpretable amplitude, we convert the peak of  $\hat{E}^X(\hat{\mathbf{d}})$  into a mean rotation angle  $\theta_{\text{IA}}$  using the minimal alignment model in App. D, Eq. (3), which assumes a nearly uniform departure from random PAs with the same semi-axis aligned to  $\hat{\mathbf{d}}_{\text{IA}}$  (major for BD, minor for DD). This mapping serves only to set the units: the detection itself is model-agnostic with respect to direction, driven by the location of the maximum of  $\hat{E}$ , its stability across spatial and redshift splits, and the spatial block bootstrap uncertainties. Our fo-

cus is a phenomenological test for dipolar alignment, not detailed modeling, and alternative monotonic mappings would merely rescale  $\theta_{IA}$ , leaving the preferred direction and the qualitative physical interpretation unchanged.

#### IV. CONCLUSIONS

We reported the first detection of a large-scale axial intrinsic alignment (LAIA): bulge-dominated semi-major axes and disk-dominated semi-minor axes are coherently oriented toward a common direction, with amplitudes obeying the hierarchy expected from tidal-torque physics. The signal persists across several spatial and redshift splits, survives PSF and lensing-leakage calibrations, as well as early/late-type misclassification mitigation, and is difficult to reconcile with survey artifacts, which would need to conspire to align bulge major axes and disk minor axes simultaneously, i.e., with a specific  $90^\circ$  phase difference. A residual systematic that rotates both samples in phase cannot, however, be completely excluded. It would mainly bias the recovered preferred direction while leaving the coherent, morphology-dependent axial pattern, and hence our qualitative conclusions, intact. Taken together, these results establish intrinsic alignments on dipolar angular scales, elevating IA from a localized, environment-driven phenomenon to a genuinely cosmological observable.

A conservative interpretation is that LAIA traces a long-wavelength tidal field seeded by primordial inhomogeneities and coherently acting on galaxies across horizon-scale modes. In this view, galaxies are not merely points sampling a density field, but oriented tracers whose vector degrees of freedom encode information about the large-scale gravitational potential. Our detection opens this “galactic cosmology” avenue: an orientation field that complements number counts and shear, and can be confronted with theory and simulations. While our conversion of the estimator peak into a mean rotation angle is a minimal, somewhat naive calibration, the preferred direction and morphology-dependent orthogonality are robust empirical facts. Notably, the lack of alignment with the CMB dipole, large-scale anomaly axes, prominent voids, or nearby attractors indicates that LAIA is not a re-detection of a known feature.

The path forward is clear. Higher-resolution, wide-area imaging with improved PSF control and morphological purity, e.g., from CSST, LSST and *Euclid*, will sharpen position-angle measurements and enable tomographic LAIA maps to test redshift evolution. On the theory side, hydrodynamical simulations and semi-analytic models should be extended to predict axial alignments on horizon-scale modes, connecting the amplitude hierarchy of bulges and disks to tidal-torque expectations and reionization-era physics. Cross-correlations of LAIA with weak-lensing shear, CMB lensing and forthcoming 21 cm tracers will provide independent checks on systematics and help isolate the underlying tidal field. Also, a

few mild tensions in our splits merit investigation with improved data and simulations. By turning galaxy orientations into a precision probe on the largest scales, LAIA offers a bridge between galaxy evolution and cosmology and a new way to test cosmic statistical isotropy.

#### ACKNOWLEDGMENTS

We thank Dr. Chihway Chang for the many insightful discussions that greatly enriched this study, and Dr. Ting-Yun Cheng for generously granting us access to her galaxy morphology catalog. We are also grateful to Dr. Marco Gatti, Dr. Erin Sheldon and Dr. Björn Malte Schäfer for their helpful comments. **Funding:** PDSF thanks Brazilian funding agency FINEP/FACC (contract 01.22.0505.00) for financial support. ROR thanks PIBIC/CNPq for financial support. PSF thanks Brazilian funding agency CNPq for financial support PCI-DB 316199/2025-7. VM acknowledges partial support from CNPq (Brazil) and FAPES (Brazil). AC acknowledges the FAPERJ (Brazil) grants E26/202.607/2022 and 210.371/2022(270993) and CNPq. CRB acknowledges the financial support from CNPq (316072/2021-4), FAPERJ (grants 201.456/2022 and 210.330/2022) and the FINEP/FACC (contract 01.22.0505.00). **Scientific Illustration:** Fig. 1 was commissioned by the artist “Drê Silva”. **CosmoHub:** This work has made use of CosmoHub, developed by PIC (maintained by IFAE and CIEMAT) in collaboration with ICE-CSIC. It received funding from the Spanish government (grant EQC2021-007479-P funded by MCIN/AEI/10.13039/501100011033), the EU NextGeneration/PRTR (PRTR-C17.I1), and the Generalitat de Catalunya. **Astro Data Lab:** This research uses services or data provided by the Astro Data Lab, which is part of the Community Science and Data Center (CSDC) Program of NSF NOIRLab. NOIRLab is operated by the Association of Universities for Research in Astronomy (AURA), Inc. under a cooperative agreement with the U.S. National Science Foundation. **Sci-Com cluster:** The authors would like to acknowledge the use of the computational resources provided by the **Sci-Com Lab** of the Department of Physics at UFES, which was funded by FAPES, CAPES, and CNPq. **Milliways HPC IF-UFRJ:** This work made use of the Milliways HPC computer located at the Instituto de Física in the Universidade Federal do Rio de Janeiro, managed and funded by **ARCOS** (Astrophysics, Relativity and COSmology research group). **LRG HPC:** This work made use of the LRG HPC computer, which was funded by FAPERJ (E-26/210.371/2022). **CHE/Milliways cluster:** We acknowledge the use of the computational resources of the joint CHE/Milliways cluster, supported by a FAPERJ grant E-26/210.130/2023. **Shape Catalog:** This work made use of the DES shape catalog [44]. **DES:** This project used public archival data from the Dark Energy Survey (DES). Funding for the DES Projects has been

provided by the U.S. Department of Energy, the U.S. National Science Foundation, the Ministry of Science and Education of Spain, the Science and Technology Facilities Council of the United Kingdom, the Higher Education Funding Council for England, the National Center for Supercomputing Applications at the University of Illinois at Urbana-Champaign, the Kavli Institute of Cosmological Physics at the University of Chicago, the Center for Cosmology and Astro-Particle Physics at the Ohio State University, the Mitchell Institute for Fundamental Physics and Astronomy at Texas A&M University, Financiadora de Estudos e Projetos, Fundação Carlos Chagas Filho de Amparo à Pesquisa do Estado do Rio de Janeiro, Conselho Nacional de Desenvolvimento Científico e Tecnológico and the Ministério da Ciência, Tecnologia e Inovação, the Deutsche Forschungsgemeinschaft, and the Collaborating Institutions in the Dark Energy Survey. The Collaborating Institutions are Argonne National Laboratory, the University of California at Santa Cruz, the University of Cambridge, Centro de Investigaciones Energéticas, Medioambientales y Tecnológicas-Madrid, the University of Chicago, University College London, the DES-Brazil Consortium, the University of Edinburgh, the Eidgenössische Technische Hochschule (ETH) Zürich, Fermi National Accelerator Laboratory, the University of Illinois at Urbana-Champaign, the Institut de Ciències de l’Espai (IEEC/CSIC), the Institut de Física d’Altes Energies, Lawrence Berkeley National Laboratory, the Ludwig-Maximilians Universität München and the associated Excellence Cluster Universe, the University of Michigan, the National Optical Astronomy Observatory, the University of Nottingham, The Ohio State University, the OzDES Membership Consortium, the University of Pennsylvania, the University of Portsmouth, SLAC National Accelerator Laboratory, Stanford University, the University of Sussex, and Texas A&M University. Based in part on observations at Cerro Tololo Inter-American Observatory, National Optical Astronomy Observatory, which is operated by the Association of Universities for Research in Astronomy (AURA) under a cooperative agreement with the National Science Foundation.

## DATA AVAILABILITY

All data is available on [cosmohub.pic.es](https://cosmohub.pic.es) (DES Y3 weak lensing shape catalog and DES Y3 GOLD catalog), [data-lab.noirlab.edu](https://data-lab.noirlab.edu) (DES Y3 GOLD cutouts and BUZZARD simulation), and [des.ncsa.illinois.edu/releases/y3a2/gal-morphology](https://des.ncsa.illinois.edu/releases/y3a2/gal-morphology) (morphological classifications). The final selected samples are available [here](#).

## CODE AVAILABILITY

Python code for the estimator and mock-generation pipeline is hosted at [github.com/pdsferreira/laia](https://github.com/pdsferreira/laia).

## AUTHOR CONTRIBUTIONS

PDSF conceived the study; developed the estimator, methodology, and code; performed the statistical analysis; contributed to the interpretation; drafted the manuscript; and assembled the data products. ROR co-developed the estimator and code and contributed to drafting the manuscript. PSF contributed to the statistical analysis and interpretation, performed visual inspection of 10 000 galaxies, critically revised the manuscript, and helped produce the data products. AC advised on and assisted with the visual-inspection protocol, contributed to the galaxy-classification pipeline, and helped define the quality-cut criteria. FF performed MORFOMETRYKA-based consistency checks of position angles and World Coordinate System solutions. VM provided independent methodological scrutiny and robustness checks, contributed to the interpretation, and critically revised the manuscript. CRB critically revised the manuscript.

## Appendix A: Data

We start with the DES Y3 shape catalog [44], applying all weak-lensing quality cuts used by the DES Collaboration [44] together with the high-purity galaxy criteria from the DES Y3 GOLD sample [45]. In addition, we impose a threshold on the position-angle (PA) uncertainty,  $\sigma_\theta < 5^\circ$ , to avoid possible residual PSF bias in galaxies with ellipticity  $\sim 1$  and other artifacts that render the PA fit unstable. These measurements use the `metacalibration` (MC) algorithm [44], with the unsheared ellipticity components having the PSF anisotropy deconvolved with high precision. We tested an additional galaxy-by-galaxy PSF deconvolution to remove potential MC residuals and found that it changes the results by less than 0.3%. Therefore, only the well-established MC measurements were adopted. A low-depth decision tree trained with `scikit-learn` [52], based on the visual inspection of 10 000 objects images, was used to derive simple piecewise thresholds to separate artifacts/blends from galaxies. Accordingly, we perform an extra filtering, letting only objects with  $47.3 < \text{SNR} \leq 75.2$  and  $T_{\text{GAL}}/T_{\text{PSF}} \leq 4.1$ , and  $T_{\text{GAL}}/T_{\text{PSF}} \leq 15.7$  if  $\text{SNR} > 75.2$ , which we found to be a simple and effective quality cut to reduce galaxy misclassification, as artifacts (mainly due to the high-SNR constraint) and blended objects (by limiting  $T_{\text{GAL}}/T_{\text{PSF}}$ ).

We divided the latter in two samples, disk-dominated galaxies and bulge-dominated galaxies, as the IA mechanisms are different, each one using specific extra quality cuts. See Fig. 2 for the density HEALPix [47] map distribution of each sample, and Fig. 3 for the redshift distribution. Using these images, we also performed a comparison between the PA measured visually, using the software MORFOMETRYKA [46] and by MC to ensure we used the correct reference frame (World Coordinate System) and if the PA are compatibles, see Fig. 5 for the deviations between different PA measurements.

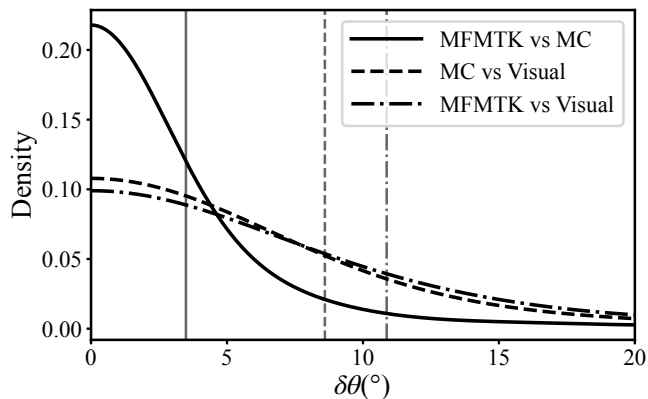


Figure 5. Distribution of position-angle differences,  $\delta\theta$ , for a sample of 10,000 galaxies, comparing MORFOMETRYKA (MFMTK), *metacalibration* (MC), and visual inspection. Vertical lines indicate the 68.27% ( $1\sigma$ ) upper bound for each distribution. MFMTK and visual inspection use only the  $I$  band, whereas *metacalibration* combines the  $R$ ,  $I$ , and  $Z$  bands to estimate the PA.

For the disk-dominated sample (DS) we consider only galaxies with robust late-type classifications by both Vega-Ferrero *et al.* [32] and Cheng *et al.* [33], bulge-to-total fraction (BDF) less than or equal to 0.5, axis ratio  $b/a \leq 0.875$  and  $a/b < 10$  (to avoid thin streak artifacts), size ratio between the galaxy and the PSF  $T_{\text{GAL}}/T_{\text{PSF}} \geq 2$ , and  $0 < z \leq 0.9$ , yielding a final DS of 3 007 638 galaxies. The  $b/a$  cut removes nearly round objects for which the PA is ill-defined and noise-dominated, this reduces PA scatter without selecting any preferred angle. The  $a/b$  veto excludes pathologically elongated detections, typically trails, blended objects, and other artifacts. These filters operate only on scalar elongation measures and are therefore PA-agnostic. The  $T_{\text{GAL}}/T_{\text{PSF}} \geq 2$  requirement ensures the galaxy is sufficiently resolved so that the PA is not driven by PSF anisotropy or model priors. Because late-type IA is intrinsically weak, these stricter PA-quality cuts reduce noise without biasing the measurement.

For the bulge-dominated sample (BS) we consider galaxies robustly classified as early-type by either Vega-Ferrero *et al.* [32] or Cheng *et al.* [33],  $\text{BDF} > 0.5$ ,  $b/a \leq 0.95$ ,  $a/b < 10$ , and  $0 < z \leq 0.9$ . Since the IA signal for ellipticals is roughly an order of magnitude larger than for disks, the  $b/a$  threshold can be relaxed to gain statistics without materially degrading PA fidelity, obtaining a final DS of 1 381 049 galaxies.

Note that no selection uses any function of PA, all are built from rotation-invariant scalars (axis ratio  $b/a$ , elongation  $a/b$ , and the resolution factor  $T_{\text{GAL}}/T_{\text{PSF}}$ ). None of these depends on the position angle itself, so they cannot imprint or prefer any sky direction. They only modulate the PA S/N. The cuts trade noise and artifacts for stability, without coupling to the LAIA signal itself.

## Appendix B: Axial alignment estimators

We obtain the galaxy’s sightline unit vector  $\hat{n}$  on the celestial sphere from the equatorial coordinate system, RA ( $\alpha$ ) and Dec ( $\delta$ ):

$$\hat{n} = \begin{bmatrix} \cos(\delta) \cos(\alpha) \\ \cos(\delta) \sin(\alpha) \\ \sin(\delta) \end{bmatrix}. \quad (\text{B1})$$

In order to build a plane tangent to the celestial sphere whose center coincides with the galaxy’s coordinates (image plane), we can use an orthonormal basis:

$$\beta = \left\{ \hat{\delta} = \frac{1}{\|\frac{\partial \hat{n}}{\partial \delta}\|} \frac{\partial \hat{n}}{\partial \delta}, \hat{\alpha} = \frac{1}{\|\frac{\partial \hat{n}}{\partial \alpha}\|} \frac{\partial \hat{n}}{\partial \alpha} = \frac{1}{\cos \delta} \frac{\partial \hat{n}}{\partial \alpha} \right\} \quad (\text{B2})$$

Therefore, we can describe any vector on the plane as a linear combination of the vectors in this basis. The galaxy’s image is a two-dimensional projection on the tangent plane. This means the semi-major axis direction of an elliptical galaxy ( $\hat{\mathbf{a}}$ ) or the semi-minor axis of a spiral galaxy ( $\hat{\mathbf{b}}$ ) can be written as a linear combination of the orthonormal basis  $\beta$ :

$$\hat{\mathbf{a}}(\alpha, \delta, \theta) = \sin \theta \hat{\delta} - \cos \theta \hat{\alpha} \quad (\text{B3})$$

$$\hat{\mathbf{b}}(\alpha, \delta, \theta) = \sin \theta \hat{\alpha} + \cos \theta \hat{\delta} \quad (\text{B4})$$

where  $\theta$  denotes the angle of the galaxies’ semi-major axis from the west ( $\theta=0 \Rightarrow \hat{\mathbf{a}} = -\hat{\alpha}$ ), measured counterclockwise.

We want to find an axial IA w.r.t. a direction  $\hat{\mathbf{d}}$ , in other words, we are insensitive to the sign of the projections  $\hat{\mathbf{d}} \cdot \hat{\mathbf{a}}_i$  ( $\hat{\mathbf{d}} \cdot \hat{\mathbf{b}}_i$ ). Since the semi-axes define axial (headless) directions rather than polar vectors, we identify  $\hat{\mathbf{a}}_i \equiv -\hat{\mathbf{a}}_i$  and  $\hat{\mathbf{b}}_i \equiv -\hat{\mathbf{b}}_i$ . Consequently, the estimator uses squared projections,  $(\hat{\mathbf{d}} \cdot \hat{\mathbf{a}}_i)^2$  and  $(\hat{\mathbf{d}} \cdot \hat{\mathbf{b}}_i)^2$ . Thus, the LAIA of a given galaxy set can be measured with an estimator  $\hat{E}(\hat{\mathbf{d}})$  that is a weighted average of the projections w.r.t.  $\hat{\mathbf{d}}$ , with weights related to  $\sigma_\theta$ :

$$\hat{E}^{\text{a}}(\hat{\mathbf{d}}) = \sum_{i=1}^{N_{\text{gal}}} \frac{w_i (\hat{\mathbf{d}} \cdot \hat{\mathbf{a}}_i)^2}{1 - (\hat{\mathbf{d}} \cdot \hat{\mathbf{n}}_i)^2} \quad \text{and} \quad \hat{E}^{\text{b}}(\hat{\mathbf{d}}) = \sum_{i=1}^{N_{\text{gal}}} \frac{w_i (\hat{\mathbf{d}} \cdot \hat{\mathbf{b}}_i)^2}{1 - (\hat{\mathbf{d}} \cdot \hat{\mathbf{n}}_i)^2}, \quad (\text{B5})$$

where “a” is the upper-index for the semi-major vector  $\hat{\mathbf{a}}$  projection, used to estimate the LAIA for bulge-dominated samples, and “b” for the semi-minor vector  $\hat{\mathbf{b}}$  projection, used to estimate the alignment in disk-dominated samples. The weights  $w_i$  are written as:

$$w_i = \frac{\sigma_{\theta,i}^{-2}}{\sum_{j=1}^{N_{\text{gal}}} \sigma_{\theta,j}^{-2}}. \quad (\text{B6})$$

The  $\sigma_{\theta,i}$  is the error in the PA (App. C). The  $1 - (\hat{\mathbf{d}} \cdot \hat{\mathbf{n}}_i)^2$  term comes from the  $\hat{\mathbf{d}}$  projection over the tangent plane

defined by  $\beta$  and renormalization. We measure  $\hat{E}^X(\hat{\mathbf{d}})$ ,  $X = \{a, b\}$ , for different  $\hat{\mathbf{d}}$  in a grid (HEALPix) following a gradient ascent optimization algorithm. The direction in which  $\hat{E}^X(\hat{\mathbf{d}})$  is maximum is the LAIA direction,  $\hat{\mathbf{d}}_{\text{IA}}$ .

As derived in App. D, by considering a simple model, with a nearly homogeneous rotation of the galaxies in all observable Universe, we can find the average rotation angle  $\theta_{\text{IA}}$  w.r.t.  $\hat{\mathbf{d}}_{\text{IA}}$ , the amplitude of the LAIA effect, given by:

$$2\theta_{\text{IA}} + 2\sin(2\theta_{\text{IA}}) = \frac{2\pi}{\bar{C}} \left( \hat{E}^X(\hat{\mathbf{d}}_{\text{IA}}) - \frac{1}{2} \right). \quad (\text{B7})$$

This is a transcendental equation that must be solved numerically. Here  $\bar{C} = \sum_{i=1}^{N_{\text{gal}}} w_i e^{-2\sigma_{\theta,i}^2}$ .

### Appendix C: From shear measurements to galaxy position angle

For a galaxy whose two-dimensional brightness distribution can be approximated by an elliptical profile, the position angle  $\theta$  can be written as function of the ellipticity parameters  $e_1$  and  $e_2$  as:

$$\theta = \frac{1}{2} \arctan 2(e_2, e_1), \quad (\text{C1})$$

where  $\arctan 2(y, x)$  is the two-argument arctangent that returns values in the range  $(-\pi, \pi]$ . Let  $\Sigma_{(e_1, e_2)}$  be the  $2 \times 2$  covariance matrix of the ellipticity parameters:

$$\Sigma_{(e_1, e_2)} = \begin{pmatrix} \sigma_{e_1}^2 & \text{Cov}(e_1, e_2) \\ \text{Cov}(e_1, e_2) & \sigma_{e_2}^2 \end{pmatrix}. \quad (\text{C2})$$

We wish to propagate this uncertainty of  $\theta$ . First note that the gradient of  $\theta$  (with respect to  $e_1$  and  $e_2$ ) is

$$\nabla\theta = \begin{pmatrix} \frac{1}{2} \frac{\partial}{\partial e_1} \arctan 2(e_2, e_1) \\ \frac{1}{2} \frac{\partial}{\partial e_2} \arctan 2(e_2, e_1) \end{pmatrix} = \begin{pmatrix} -\frac{e_2}{2(e_1^2 + e_2^2)} \\ \frac{e_1}{2(e_1^2 + e_2^2)} \end{pmatrix}. \quad (\text{C3})$$

Using standard error propagation for correlated variables, the variance of  $\theta$  is given by

$$\sigma_{\theta}^2 = \nabla\theta^T \Sigma_{(e_1, e_2)} \nabla\theta, \quad (\text{C4})$$

we obtain

$$\sigma_{\theta}^2 = \frac{[e_2^2 \sigma_{e_1}^2 + e_1^2 \sigma_{e_2}^2 - 2e_1 e_2 \text{Cov}(e_1, e_2)]}{4(e_1^2 + e_2^2)^2}. \quad (\text{C5})$$

In practice, we impose a  $1^\circ$  lower bound to stabilize the weighting ( $\sigma_{\theta,i} \rightarrow \max(\sigma_{\theta,i}, 1^\circ)$ ). This choice reflects our focus on a global dipole estimate rather than dominance by a few high-SNR objects.

### Appendix D: How to compute $\theta_{\text{IA}}$

We start assuming that the measurement error  $\delta_i$  follows a Gaussian distribution with standard deviation  $\sigma_{\theta,i}$  (which was previously called as the PA error), its probability density function is:

$$P_i(\delta) = \frac{1}{\sqrt{2\pi} \sigma_{\theta,i}} e^{-\delta^2 / (2\sigma_{\theta,i}^2)}. \quad (\text{D1})$$

We can now expand the scalar product of the estimator in terms of the angle between the vectors  $\hat{\mathbf{d}}$  and  $\hat{\mathbf{a}}_i$ ,  $\phi_i$ :

$$\begin{aligned} (\hat{\mathbf{d}} \cdot \hat{\mathbf{a}}_i)^2 &= \cos^2(\phi_i + \delta_i) = \frac{1}{2} + \frac{1}{2} \cos(2(\phi_i + \delta_i)) \\ &= \frac{1}{2} [1 + \cos(2\phi_i) \cos(2\delta_i) - \sin(2\phi_i) \sin(2\delta_i)]. \end{aligned} \quad (\text{D2})$$

Such that the average is given by

$$\begin{aligned} \langle (\hat{\mathbf{d}} \cdot \hat{\mathbf{a}}_i)^2 \rangle &= \frac{1}{2} + \frac{1}{2} \langle \cos(2\phi_i) \cos(2\delta_i) \rangle_{\phi, \delta} \\ &= \frac{1}{2} + \frac{C_i}{2} \langle \cos(2\phi_i) \rangle_{\phi}. \end{aligned} \quad (\text{D3})$$

Where  $C_i$  measures the IA attenuation due to  $\sigma_{\theta,i}$ . The  $C_i$  is computed as an average of  $\cos(2\delta_i)$  over this distribution:

$$C_i = \langle \cos 2\delta_i \rangle_{\delta} = \int_{-\infty}^{\infty} \cos(2\delta) P_i(\delta) d\delta = e^{-2\sigma_{\theta,i}^2}. \quad (\text{D4})$$

Thus,  $C_i$  varies from 1 (perfectly preserved alignment) to 0 (signal totally lost by noise). We can do the same with  $\hat{\mathbf{b}}_i$ . We should also consider the ‘‘saturation’’ effect of the average rotation introduced by the IA. In other words, if the average rotation is  $\theta_{\text{IA}}$ , when a galaxy have  $\phi_i < \theta_{\text{IA}}$ , it rotates less than the average rotation to find the alignment direction. Considering a Universe without LAIA, a galaxy would have a random angular distance  $\phi_i$ , with LAIA it would have  $\phi'_i$  given by:

$$\phi'_i = \begin{cases} 0, & 0 \leq \phi < \theta_{\text{IA}}, \\ \phi - \theta_{\text{IA}}, & \theta_{\text{IA}} \leq \phi \leq \frac{\pi}{2}. \end{cases} \quad (\text{D5})$$

Assuming a homogeneous distribution of the angular distance of galaxies without LAIA, we find that the probability density is  $K(\phi) = 2/\pi$ . With LAIA:

$$\begin{aligned} \langle \cos(2\phi'_i) \rangle &= \int_0^{\pi/2} \cos(2\phi'_i) K(\phi) d\phi \\ &= \frac{2}{\pi} \left[ \int_0^{\theta_{\text{IA}}} 1 d\phi + \int_{\theta_{\text{IA}}}^{\pi/2} \cos(2\phi - \theta_{\text{IA}}) d\phi \right] \\ &= \frac{2}{\pi} \left[ \theta_{\text{IA}} + \frac{1}{2} \sin(2\theta_{\text{IA}}) \right]. \end{aligned} \quad (\text{D6})$$

Therefore,

$$\langle (\hat{\mathbf{d}} \cdot \hat{\mathbf{a}}_i)^2 \rangle = \frac{1}{2} + \frac{C_i}{\pi} \left[ \theta_{\text{IA}} + \frac{1}{2} \sin(2\theta_{\text{IA}}) \right]. \quad (\text{D7})$$

As a result, we can estimate the average rotation angle of the galaxies w.r.t.  $\hat{\mathbf{d}}_{\text{IA}}$  through:

$$\hat{E}^{\text{X}}(\hat{\mathbf{d}}_{\text{IA}}) = \frac{1}{2} + \frac{\bar{C}}{\pi} \left[ \theta_{\text{IA}} + \frac{1}{2} \sin(2\theta_{\text{IA}}) \right], \quad (\text{D8})$$

where

$$\bar{C} = \sum_{i=1}^{N_{\text{gal}}} w_i C_i. \quad (\text{D9})$$

Finally, the equation for  $\theta_{\text{IA}}$  is:

$$2\theta_{\text{IA}} + 2 \sin(2\theta_{\text{IA}}) = \frac{2\pi}{\bar{C}} \left( \hat{E}^{\text{X}}(\hat{\mathbf{d}}_{\text{IA}}) - \frac{1}{2} \right), \quad (\text{D10})$$

which is a transcendental equation.

### Appendix E: Lensing leakage

Our estimator is axial (even under  $\hat{\mathbf{n}} \rightarrow -\hat{\mathbf{n}}$ , i.e. antipodal symmetry) and therefore responds only to even-parity structure on the sky. In an ideal, isotropic full-sky survey, weak lensing, a spin-2 field, does not generate a net axial dipole that could mimic our large-scale signal. In real data, however, lensing couples to survey anisotropies: shear induces small rotations of galaxy position angles, while magnification modulates the sample and the effective weights across the footprint. Through an incomplete and anisotropic mask, these coherent but small perturbations may not cancel and can shift the location of the axial maximum, we refer to this as a lensing leakage.

To assess this effect, we used the BUZZARD  $N$ -body lightcone with ray tracing, selecting 55 million galaxies in the same redshift range and applying the DES footprint (rotated to the simulation quadrant for consistency). We ran the alignment pipeline twice, once with lensing applied to the measured position angles and once without. The recovered average rotation,  $\theta_{\text{IA}}$ , differs by  $1' \pm 0.2'$ .

In practice, although this is a small effect, we model the lensing-footprint coupling as a stochastic axial rotation: the amplitude is fixed by the BUZZARD calibration, while the direction is unknown a priori. Accordingly, in each simulation or bootstrap resampling we apply an additional axial rotation of  $1'$  in a random isotropically distributed direction. This procedure inflates the error bars to capture the realistic, footprint-mediated, impact of lensing on our estimator.

### Appendix F: PSF leakage on large angular scales

Although `metacalibration` strongly suppresses PSF-anisotropy leakage, residual large-scale modes can remain. To remove it we adopt a linear model with respect

to the centered maps ( $\tilde{E} \equiv E - \langle E \rangle$ )

$$\tilde{E}_{\text{OBS}}^{\text{X}}(\hat{\mathbf{d}}) = \tilde{E}_{\text{IA}}^{\text{X}}(\hat{\mathbf{d}}) + \eta_{\text{R}}^{\text{X}} \tilde{E}_{\text{PSF}}^{\text{X}}(\hat{\mathbf{d}}), \quad (\text{F1})$$

where  $\hat{\mathbf{d}}$  runs over the tested directions (HEALPix centers at NSIDE=32), with  $\text{X} = \{\text{a}, \text{b}\}$ ,  $E_{\text{OBS}}$  is obtained from Eq. (1) using observed data,  $E_{\text{PSF}}$  is the same estimator built from PSF semi-axes, and  $E_{\text{IA}}$  is the PSF-unbiased signal. We estimate  $\eta_{\text{R}}^{\text{X}}$  by least squares,

$$\eta_{\text{R}}^{\text{X}} = \arg \min_{\eta_{\text{R}}^{\text{X}}} \left\langle [\tilde{E}_{\text{OBS}}^{\text{X}} - \eta_{\text{R}}^{\text{X}} \tilde{E}_{\text{PSF}}^{\text{X}}]^2 \right\rangle, \quad (\text{F2})$$

or equivalently

$$\eta_{\text{R}}^{\text{X}} = \frac{\text{Cov}(\tilde{E}_{\text{OBS}}^{\text{X}}, \tilde{E}_{\text{PSF}}^{\text{X}})}{\text{Var}(\tilde{E}_{\text{PSF}}^{\text{X}})}, \quad (\text{F3})$$

provided  $\text{Var}(\tilde{E}_{\text{PSF}}^{\text{X}}) > 0$ . After de-leakage we compute  $\hat{\mathbf{d}}_{\text{IA}}$  and  $\theta_{\text{IA}}$  from  $E_{\text{IA}}$ . The detected large scale lensing leakage amplitude was  $\eta_{\text{R}}^{\text{X}} \simeq 0.05$ .

Essentially, we remove PSF leakage by orthogonalizing the observed, mean-subtracted map against the PSF template. Because the true IA field is expected to be statistically uncorrelated with instrumental PSF patterns, this projection removes only the PSF-colinear component and is unbiased in expectation.

### Appendix G: Misclassification bias

The contamination fraction  $\kappa$  was obtained as the average of the probability of the galaxies being late-type (disc-dominated) or early-type (bulge-dominated) from two different algorithms, we name the probabilities  $P^{\text{V}}$  obtained by Vega-Ferrero *et al.* [32] and  $P^{\text{C}}$  by Cheng *et al.* [33]:

$$\kappa^{\text{Y}} = 1 - \sum_{i=1}^{N_{\text{gal}}^{\text{Y}}} \frac{P_i^{\text{V}, \text{Y}} + P_i^{\text{C}, \text{Y}}}{2N_{\text{gal}}^{\text{Y}}}, \quad (\text{G1})$$

where  $\text{Y} = \{l, e\}$ , for late-type ( $l$ ) and early-type ( $e$ ). We estimate 0.27% of contamination for disk-dominated galaxies (in DD). The BD contamination is much bigger, 26.55%. In order to understand this difference, it is important to notice that both [32] and [33] deep learning methods are trained using Galaxy Zoo visual morphology, which relies on the ability of humans to identify patterns on images. Spiral structures are readily recognized through visual inspection up to a given threshold, for example missing faint spiral structures. Moreover, lenticular galaxies, which are characterized by a disk and a prominent bulge, can be associated to both early and late type class. In few words, while the late type class encompass all objects with visible spiral arms, the early type class might contain elliptical galaxies, lenticular galaxies, multiple object images, low surface brightness galaxies, bulge-dominated spiral galaxies, or faint/compact spiral

galaxies, in different numbers in the two papers, resulting in a higher number of discordant classification and, therefore, a bigger associated error [53, 54].

Given  $\kappa^Y$  one can show that the relation between the biased  $E^a$  ( $E_{\text{biased}}^a$ ) and the unbiased  $E^a$  is

$$E_{\text{biased}}^a = \frac{1}{N_{\text{gal}}} \left( \sum_{i=1}^{(1-\kappa^e)N_{\text{gal}}} w_i (\hat{\mathbf{d}} \cdot \hat{\mathbf{a}}_i^{\text{b}})^2 + \sum_{i=1}^{\kappa^e N_{\text{gal}}} w_i (\hat{\mathbf{d}} \cdot \hat{\mathbf{a}}_i^{\text{d}})^2 \right),$$

$$\simeq (1 - \kappa^e) E^a, \quad (\text{G2})$$

When measuring the LAIA of the semi-major axis in the BS. Equivalently, for the LAIA of the semi-minor axis in the DS:

$$E_{\text{biased}}^{\text{b}} \simeq (1 - \kappa^l) E^{\text{b}}. \quad (\text{G3})$$

This is valid because the value of  $\langle (\hat{\mathbf{d}}_{\text{IA}} \cdot \hat{\mathbf{a}})^2 \rangle$  is not significant for disk-dominated galaxies, and similarly  $\langle (\hat{\mathbf{d}}_{\text{IA}} \cdot \hat{\mathbf{b}})^2 \rangle$  is null for bulge-dominated galaxies, i.e. the misclassified population is on average perpendicular to the alignment direction of the dominant population.

### Appendix H: Mock generation

We verify the estimator and obtain null statistics with mock catalogs. Each realization reproduces the angular distribution of the data (Fig. 2) and the per-object PA uncertainties, while injecting a controlled axial IA signal about a fixed sky direction  $\hat{\mathbf{d}}_{\text{IA}}$ . We first sample galaxy directions  $\hat{\mathbf{n}}_i$  from the observed density map and, for each object, draw an intrinsic position angle  $\theta_i \sim \mathcal{U}(0, \pi)$ , constructing the orthonormal tangent-plane semi-axes  $\hat{\mathbf{a}}_i(\theta_i)$  and  $\hat{\mathbf{b}}_i(\theta_i)$  as in Eq. B3. For every sky position we then project the IA axis onto the local tangent plane,

$$\hat{\mathbf{d}}_i^{\text{proj}} \equiv \frac{\hat{\mathbf{d}}_{\text{IA}} - (\hat{\mathbf{d}}_{\text{IA}} \cdot \hat{\mathbf{n}}_i) \hat{\mathbf{n}}_i}{\|\hat{\mathbf{d}}_{\text{IA}} - (\hat{\mathbf{d}}_{\text{IA}} \cdot \hat{\mathbf{n}}_i) \hat{\mathbf{n}}_i\|}, \quad (\text{H1})$$

and, prior to any rotation, define the initial axial separation

$$\phi_i^{\text{orig}} \equiv \arccos\left(\left|\hat{\mathbf{a}}_i \cdot \hat{\mathbf{d}}_i^{\text{proj}}\right|\right), \quad (\text{H2})$$

where the absolute value enforces the  $180^\circ$  degeneracy appropriate for an axial major axis. The rotation amplitude is limited by the saturation prescription in Eq. D5,

$$\tilde{\phi}_i \equiv \min\left(\phi_i^{\text{orig}}, \theta_{\text{IA}}\right), \quad (\text{H3})$$

and its sense on the tangent plane (clockwise/counterclockwise) follows the scalar triple product,

$$s_i \equiv \text{sgn}\left[\hat{\mathbf{n}}_i \cdot (\hat{\mathbf{a}}_i \times \hat{\mathbf{d}}_i^{\text{proj}})\right] \in \{-1, +1\}, \quad \phi'_i \equiv s_i \tilde{\phi}_i. \quad (\text{H4})$$

We then rotate  $\hat{\mathbf{a}}_i$  about  $\hat{\mathbf{n}}_i$  by  $\phi_i$  using Rodrigues' formula [55], because  $\hat{\mathbf{a}}_i \cdot \hat{\mathbf{n}}_i = 0$ , the expression reduces to

$$\hat{\mathbf{a}}_i^{\text{rot}} = \hat{\mathbf{a}}_i \cos \phi'_i + (\hat{\mathbf{n}}_i \times \hat{\mathbf{a}}_i) \sin \phi'_i. \quad (\text{H5})$$

Equivalently, we can use the same procedure to obtain the rotated semi-minor axis. Measurement noise is included as an additional rotation,

$$\phi_i^{\text{noise}} \sim \mathcal{N}(0, \sigma_\theta^2(\hat{\mathbf{n}}_i)), \quad (\text{H6})$$

where  $\sigma_\theta(\hat{\mathbf{n}}_i)$  is the mean PA uncertainty in the sky pixel at  $\text{NSIDE}=128$ , containing  $\hat{\mathbf{n}}_i$ . The lensing leakage is included as an extra stochastic axial rotation of fixed amplitude (App. E). Residual large-scale PSF systematics are not injected into the mocks and are handled exclusively in the real-data analysis. For mocks used to estimate the null case statistics, we made  $\theta_{\text{IA}} = 0$ , include the angular distribution (anisotropies), mask, the PA uncertainties, and lensing leakage. See Fig. 6 for the estimator-parameter distributions obtained from mocks calibrated to the real data.

### Appendix I: Expected errors

We estimate uncertainties with a spatial block bootstrap at the HEALPix pixel level. We partition the sky into equal-area pixels ( $\text{NSIDE} = 16$ ), identify the set of occupied pixels within the survey footprint, and treat each pixel as one resampling unit. For each of realizations we sample pixels with replacement, drawing the same number of pixel as in the data from the set of occupied pixels (each pixel equally likely). For every selected pixel, we include all galaxies contained in that pixel (with their per-object uncertainties and matched PSF entry). Resampling whole pixels preserves local clustering and position-dependent selection/PSF systematics at scales bigger than the pixel size ( $\sim 3.7^\circ$ ), providing a conservative uncertainty that respects survey inhomogeneities, something an object-level bootstrap would not capture as well. To test the bootstrap procedure we rely on the mocks generated as discussed in App. H, verifying that they recover the expected value on average and similar variance.

### Appendix J: Insensitivity to redshift-space distortions

Our measurement uses only the projected PAs of galaxy images on the sky. For each galaxy we rely on its angular position and the PA of its semi-axis measured in the plane perpendicular to the line of sight. The estimator correlates these projected PAs with a fixed axial direction on the celestial sphere, it does not use three-dimensional positions, radial separations, or redshift-space clustering statistics.

Redshift-space distortions (RSD) act by displacing galaxies along the line of sight according to their peculiar velocities, thereby altering inferred radial distances and the anisotropy of the three-dimensional correlation function or power spectrum ( $P(k)$ ). However, this mapping

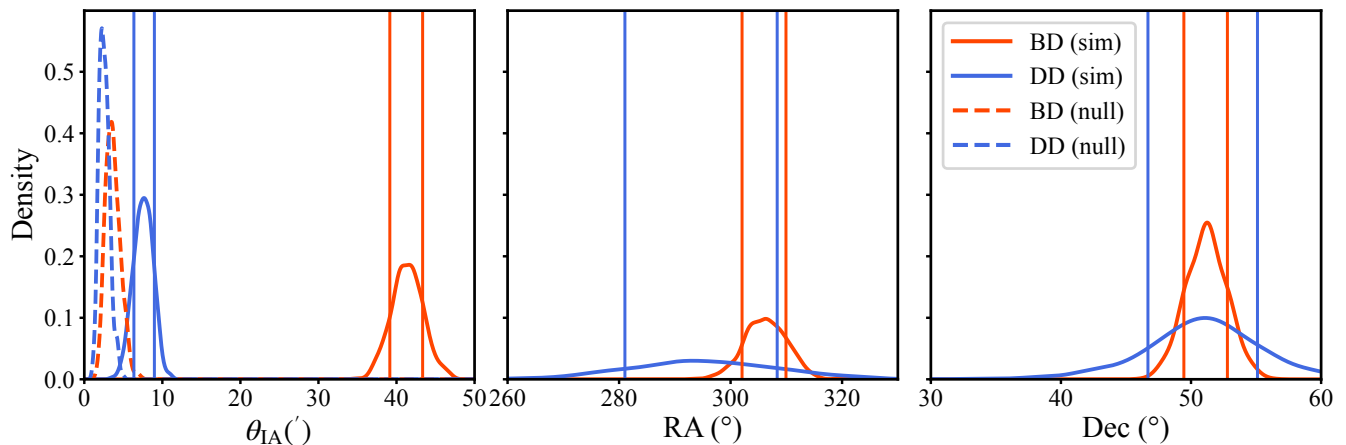


Figure 6. Mock-derived distributions of the estimator parameters, calibrated to the real-data estimates for BD and DD. Solid curves correspond to 500 signal-injected mocks, dashed curves to 500 null mocks including lensing leakage. Vertical lines indicate the 68.27% HDIs ( $1\sigma$  equivalent).

leaves the sky coordinates and the local tangent plane unchanged. The galaxy image is always formed in the plane perpendicular to the line of sight, and shifting a galaxy along that line does not rotate the apparent orientation of its projected semi-axis in that plane.

It is therefore useful to distinguish between radial orientation effects and the projected PAs we use. Many RSD-related systematics depend only on how strongly a galaxy is oriented towards or away from the observer (its inclination), and are symmetric around the line of sight. Such effects change the distribution of inclinations and apparent axis ratios, but they do not single out any preferred direction within the sky plane. As a result, they cannot generate a coherent large-scale pattern in PAs relative to a fixed direction on the sky, which would be required to mimic our axial intrinsic-alignment signal. For example, the orientation-dependent selection effect studied by Lamman *et al.* [56] modifies the relative abundance of galaxies as a function of inclination and thus the redshift-space multipoles, but it does not imprint any preferred PA direction within the sky plane. Conversely, Lamman *et al.* [57] show that suitably projected IA estimators in spectroscopic surveys can be constructed to be explicitly insensitive to RSD. Our PA-based measurement is an even more extreme case, as it is defined purely on the sky plane and does not involve line-of-sight separations.

In practice, inclination-dependent selection effects associated with redshift surveys mainly affect our analysis through sample definition. Galaxies whose symmetry axis is closely aligned with the line of sight appear nearly round and have poorly constrained PAs, these objects are naturally down-weighted or removed by our cuts in resolution and ellipticity. This reduces the effective number density and slightly reshapes the distribution of apparent ellipticities, but it does not correlate the surviving PAs with any particular sky direction. RSD therefore

act primarily by limiting the usable sample, rather than by inducing a spurious axial pattern in the projected orientation field.

- [1] N. E. Chisari, *Astron. Astrophys. Rev.* **33**, 5 (2025), arXiv:2510.15738 [astro-ph.CO].
- [2] C. Lamman *et al.* 10.21105/astro.2309.08605 (2023), arXiv:2309.08605 [astro-ph.CO].
- [3] C. M. Hirata and U. Seljak, *Phys. Rev. D* **70**, 063526 (2004), [Erratum: *Phys.Rev.D* 82, 049901 (2010)], arXiv:astro-ph/0406275.
- [4] B. Joachimi *et al.*, *Space Sci. Rev.* **193**, 1 (2015), arXiv:1504.05456 [astro-ph.GA].
- [5] M. A. Troxel and M. Ishak, *Phys. Rept.* **558**, 1 (2014), arXiv:1407.6990 [astro-ph.CO].
- [6] R. G. Crittenden, P. Natarajan, U.-L. Pen, and T. Theuns, *Astrophys. J.* **559**, 552 (2001), arXiv:astro-ph/0009052.
- [7] J. Blazek, Z. Vlah, and U. Seljak, *JCAP* **08**, 015, arXiv:1504.02510 [astro-ph.CO].
- [8] N. E. Chisari *et al.*, *Mon. Not. Roy. Astron. Soc.* **454**, 2736 (2015), arXiv:1507.07843 [astro-ph.CO].
- [9] S. Codis, C. Pichon, and D. Pogosyan, *Mon. Not. Roy. Astron. Soc.* **452**, 3369 (2015), arXiv:1504.06073 [astro-ph.CO].
- [10] A. Kiessling *et al.*, *Space Sci. Rev.* **193**, 67 (2015), [Erratum: *Space Sci.Rev.* 193, 137 (2015)], arXiv:1504.05546 [astro-ph.GA].
- [11] D. Kirk *et al.*, *Space Sci. Rev.* **193**, 139 (2015), arXiv:1504.05465 [astro-ph.GA].
- [12] K. Kraljic, R. Dave, and C. Pichon, *Mon. Not. Roy. Astron. Soc.* **493**, 362 (2020), arXiv:1906.01623 [astro-ph.GA].
- [13] S. Samuroff, R. Mandelbaum, and J. Blazek, *Mon. Not. Roy. Astron. Soc.* **508**, 637 (2021), arXiv:2009.10735 [astro-ph.CO].
- [14] J. Blazek, R. Mandelbaum, U. Seljak, and R. Nakajima, *JCAP* **2012** (5), 041, arXiv:1204.2264 [astro-ph.CO].
- [15] F. Schmidt, N. E. Chisari, and C. Dvorkin, *JCAP* **10**, arXiv:1506.02671 [astro-ph.CO].
- [16] K. Kogai *et al.*, *Journal of Cosmology and Astroparticle Physics* **2018** (08), 014.
- [17] H. Zhan, *Chinese Science Bulletin* **66**, 1290 (2021).
- [18] LSST Collaboration, *Large synoptic survey telescope: Dark energy science collaboration* (2012), arXiv:1211.0310 [astro-ph.CO].
- [19] R. Scaramella *et al.*, *Astronomy & Astrophysics* **662**, A112 (2022).
- [20] S. Hilbert *et al.*, *Mon. Not. Roy. Astron. Soc.* **468**, 790 (2017), arXiv:1606.03216 [astro-ph.CO].
- [21] M. L. Brown *et al.*, *Mon. Not. Roy. Astron. Soc.* **333**, 501 (2002), arXiv:astro-ph/0009499.
- [22] A. Smargon *et al.*, *Mon. Not. Roy. Astron. Soc.* **423**, 856 (2012), arXiv:1109.6020 [astro-ph.CO].
- [23] C. Lamman *et al.*, *Mon. Not. Roy. Astron. Soc.* **534**, 3540 (2024), arXiv:2408.11056 [astro-ph.CO].
- [24] E. Abdalla *et al.*, *JHEAp* **34**, 49 (2022), arXiv:2203.06142 [astro-ph.CO].
- [25] E. Di Valentino *et al.* (CosmoVerse), *Phys. Dark Univ.* **49**, 101965 (2025), arXiv:2504.01669 [astro-ph.CO].
- [26] K. Minato, A. Taruya, T. Okumura, and M. Shiraiishi, arXiv e-prints (2025), arXiv:2505.19941 [astro-ph.CO].
- [27] M. O. Calvao, G. I. Gomero, B. Mota, and M. J. Reboucas, *Class. Quant. Grav.* **22**, 1991 (2005), arXiv:astro-ph/0404536.
- [28] M. Bartelmann and P. Schneider, *Phys. Rept.* **340**, 291 (2001), arXiv:astro-ph/9912508.
- [29] M. A. Troxel and M. Ishak, *Physics Reports* **558**, 1 (2015), 1407.6990.
- [30] J. Blazek, M. McQuinn, and U. Seljak, *JCAP* **2011** (5), 010, arXiv:1101.4017 [astro-ph.CO].
- [31] P. Catelan, M. Kamionkowski, and R. D. Blandford, *Mon. Not. Roy. Astron. Soc.* **320**, L7 (2001), arXiv:astro-ph/0005470.
- [32] J. Vega-Ferrero *et al.* (DES), *Mon. Not. Roy. Astron. Soc.* **506**, 1927 (2021), arXiv:2012.07858 [astro-ph.GA].
- [33] T.-Y. Cheng *et al.*, *MNRAS* **507**, 4425 (2021), arXiv:2107.10210 [astro-ph.GA].
- [34] S. Bridle and L. King, *New Journal of Physics* **9**, 444 (2007).
- [35] J. A. Blazek *et al.*, *Physical Review D* **100**, 103506 (2019).
- [36] F. H. Peters *et al.*, *Astron. Astrophys.* **699**, A201 (2025), arXiv:2412.01790 [astro-ph.CO].
- [37] B. Ghosh, R. Durrer, and B. M. Schaefer, *Mon. Not. Roy. Astron. Soc.* **505**, 2594 (2021), arXiv:2005.04604 [astro-ph.CO].
- [38] M. C. Fortuna *et al.*, *Astronomy & Astrophysics* **654**, A76 (2021).
- [39] C. Georgiou *et al.*, *Astron. Astrophys.* **699**, A252 (2025), arXiv:2502.09452 [astro-ph.CO].
- [40] E. Tempel, R. S. Stoica, and E. Saar, *Monthly Notices of the Royal Astronomical Society* **428**, 1827 (2013).
- [41] J. Lee and P. Erdogdu, *The Astrophysical Journal* **671**, 1248 (2007).
- [42] A. M. Delgado *et al.*, *Monthly Notices of the Royal Astronomical Society* **523**, 5899 (2023), 2304.12346.
- [43] N. D. Padilla and M. A. Strauss, *Monthly Notices of the Royal Astronomical Society* **388**, 1321 (2008), 0802.0877.
- [44] M. Gatti *et al.* (DES), *Mon. Not. Roy. Astron. Soc.* **504**, 4312 (2021), arXiv:2011.03408 [astro-ph.CO].
- [45] I. Sevilla-Noarbe *et al.* (DES), *Astrophys. J. Suppl.* **254**, 24 (2021), arXiv:2011.03407 [astro-ph.CO].
- [46] F. Ferrari, R. R. de Carvalho, and M. Trevisan, *Astrophys. J.* **814**, 55 (2015), arXiv:1509.05430 [astro-ph.GA].
- [47] K. M. Górski *et al.*, *Astrophys. J.* **622**, 759 (2005), arXiv:astro-ph/0409513.
- [48] C.-H. To *et al.*, *Astrophys. J.* **961**, 59 (2024), arXiv:2303.12104 [astro-ph.CO].
- [49] N. Aghanim *et al.* (Planck), *Astron. Astrophys.* **641**, A1 (2020), arXiv:1807.06205 [astro-ph.CO].
- [50] D. J. Schwarz, C. J. Copi, D. Huterer, and G. D. Starkman, *Class. Quant. Grav.* **33**, 184001 (2016), arXiv:1510.07929 [astro-ph.CO].
- [51] R. Tully *et al.*, *Astrophys. J.* **880**, 24 (2019), arXiv:1905.08329 [astro-ph.CO].
- [52] F. Pedregosa *et al.*, *Journal of Machine Learning Research* **12**, 2825 (2011).
- [53] C. J. Lintott *et al.*, *Mon. Not. Roy. Astron. Soc.* **389**, 1179 (2008), arXiv:0804.4483 [astro-ph].
- [54] C. R. Bom *et al.*, *MNRAS* **528**, 4188 (2024), arXiv:2306.08684 [astro-ph.GA].
- [55] O. Rodrigues, *Journal de Mathématiques Pures et Appliquées*, 380 (1840).
- [56] C. Lamman *et al.*, *Mon. Not. Roy. Astron. Soc.* **522**, 117 (2023), arXiv:2209.03949 [astro-ph.CO].
- [57] C. Lamman, J. Blazek, and D. J. Eisenstein, arXiv preprint (2025), arXiv:2504.16076 [astro-ph.CO].